Journal of Materials Chemistry C

Unravelling the atomic mechanisms of tetrahedral doping in chalcogenide glass for electrical switching materials

Journal:	*Journal of Materials Chemistry C*
Manuscript ID	TC-ART-08-2023-002984.R1
Article Type:	Paper
Date Submitted by the Author:	03-Oct-2023
Complete List of Authors:	Gu, Rongchuan; Huazhong University of Science and Technology Xu, Meng; The University of Hong Kong, ; Liu, Yongpeng; Huazhong University of Science and Technology Shen, Yinghua; Huazhong University of Science and Technology Qiao, Chong; Huazhong University of Science and Technology, Wang, Cai Zhuang; Ames Laboratory-U.S. DOE, Physics and Astronomy Ho, Kai Ming; Ames Laboratory-U.S. DOE, Physics and Astronomy Wang, Songyou; Fudan University, Department of Optical Science and Engineering Xu, Ming; Huazhong University of Science and Technology, Miao, Xiangshui; Huazhong University of Science and Technology, Optical and Electronic Information

Unravelling the atomic mechanisms of tetrahedral doping in chalcogenide glass for electrical switching materials

Rongchuan Gu, [a, b] Meng Xu, [c, *] Yongpeng Liu, [a, b] Yinghua Shen, [a, b] Chong Qiao, [d] Cai-Zhuang Wang, [e] Kai-Ming Ho, [e] Songyou Wang, [f] Ming Xu, [a, b, *] and Xiangshui Miao [a, b]

[a] *School of Integrated Circuits, Huazhong University of Science and Technology, Wuhan 430074, China*

[b] *Hubei Yangtze Memory Laboratories, Wuhan 430205, China*

[c] *Department of Electrical and Electronic Engineering, the University of Hong Kong, Hong Kong, China*

[d] *School of Mathematics and Physics, Nanyang Institute of Technology, Nanyang 473004, China*

[e] *Ames Laboratory, U. S. Department of Energy and Department of Physics and Astronomy, Iowa State University, Ames, Iowa 50011, USA*

[f] *Shanghai Ultra-Precision Optical Manufacturing Engineering Center and Department of Optical Science and Engineering, Fudan University, Shanghai 200433, China*

*Authors to whom correspondence should be addressed: mengxu@hku.hk; mxu@hust.edu.cn

Abstract

The ovonic threshold switching (OTS) selector is crucial for the development of high-density memory devices based on three-dimensional semiconductor integration technology, as it could suppress leakage current. However, the performance of OTS materials based on chalcogenide glass is not yet satisfactory, hindering the progress of

industrial advancement. Si doping, by introducing tetrahedral sp^3 bonding into materials, is a key method to improve the thermal stability of chalcogenide glass, but the specific mechanism of such a dopant is not very clear. In this study, we investigate the effect of Si doping on the local structure, bonding nature, and electronic properties of amorphous GeSe (*a*-GeSiSe), to gain a better understanding of the doping effect. Our results suggest that Si atoms form tetrahedral motifs with stronger Si-Ge and Si-Se bonds, thus slow down atomic mobility to increase the activation energy of crystallization. Meanwhile, the resulting narrowed band gap of *a*-GeSiSe is advantageous in decreasing the threshold voltage (V_{th}). In addition, doping Si leads to stable mid-gap states thus effectively suppresses the V_{th} drift. Our study clarifies the important role of Si doping in OTS materials and facilitates the development of 3D phase-change memory.

Keywords: chalcogenide glass; Si doping; local structure; threshold switching; mid-gap states; molecular dynamics

1. Introduction

The down-scaling of semiconductor processing technology has created performance bottlenecks in traditional information memory devices, leading to the high demands of next-generation nonvolatile memories to meet the requirements of emerging artificial intelligence and neuromorphic computing. Phase-change memory (PCM), which takes advantage of the reversible and fast transition between the crystalline and amorphous states of chalcogenide materials, is the most mature and promising candidate. [1-7] Three-dimensional (3D) stacking technology has been applied in PCM, including successful commercialization of 3D XPoint technology by Intel and Micron, as an effective way to increase storage density. [8, 9] In this compact crossbar structure, each PCM unit is integrated with an ovonic threshold switching (OTS) selector to control the open and shut of this memory unit in 3D PCM integration technology, so that the leakage current is suppressed when the unit is off. [10-12] By adopting OTS selectors instead of traditional transistors, the chip structure and processing are largely simplified, and the physical

volume of memory chips can also be reduced. However, the unsatisfactory performance of OTS devices compared to transistors has severely hindered the industrial advancement of 3D PCM, and particularly, the demand for high thermal stability in OTS glass is essential, as they need to survive the backend-of-the-line (BEOL) processing temperature (~450°C) [11] and threshold switching operations; once the amorphous OTS material crystallizes, the entire unit fails and can no longer be recovered. Thus, it is urgent to develop OTS materials with superior properties. [13] However, the complexity of the amorphous structure and the inadequate understanding of OTS materials pose challenges to this goal.

The OTS behavior means that the conductivity of the device abruptly increases when a voltage bias reaches a threshold value V_{th}, and once the voltage bias is removed, the OTS material instantly returns to a low conductivity state without any phase transition or separation. Since the discovery of the threshold switching behavior in $Ge_{10}Si_{12}As_{30}Te_{48}$ in 1960s, [14] many OTS materials with similar properties have been reported, including Te-, [15-18] Se-, [18-21] and S-based [22, 23] chalcogenide glasses, depending on their anion types. The OTS behavior has attracted much attention, and a lot of efforts have been made to explore the phenomenon, [24-29] and so far, the mechanisms of threshold switching could be summarized as pure electrical model, [30, 31] thermal runaway, [32] field-induced nucleation, [33, 34] and filamentary switching [35, 36] mechanisms. Among these proposed mechanisms, the pure electrical model stands out as the most widely accepted theory which is consistent with the experimental OTS results very well, and presents a few nanoseconds switching-speed superior to other mechanisms. [19, 22, 31, 37] In this theory, the defect states or mid-gap states (MGS) located in the band gap play a critical role, [38] as the electric field tilts the energy band, promoting the localized carriers trapped by the MGS to the conduction band, leading to the threshold switching process. The origin of MGS in chalcogenide glass has been intensively studied, as it is the key to the design of new OTS materials. It was reported that the contribution of over-coordinated Ge atoms to the MGS is critical in amorphous $Ge_2Sb_2Te_5$, [27] GeSe [21] and GeS, [22] while it stems from the Te atoms in amorphous SiTe [12] and Te. [39]

Other than low thermal stability, the amorphous OTS materials usually suffer from large V_{th} drift, i.e., the V_{th} changes slowly with time or after many cycles of electrical operation, probably due to the glass ageing or phase separation. The drift coefficient is a parameter to measure how fast the V_{th} changes, and it is related to the evolution of MGS and mobility gap. [40] The increasing thermal stability of glass not only allows the OTS materials to withstand the BEOL temperature, but can also slow down the relaxation of glass, and thus, higher stability is critical for the development of OTS materials for the 3D memory stacking technology. In addition, to integrate with phase change materials (PCMs) in 3D stacking architecture, high thermal stability is also necessary for OTS materials to withstand the BEOL process. However, binary OTS materials such as Ge-Te, [41] B-Te [15] and Ge-Se [21] with weak stability fail to meet this demand. The tetrahedral doping strategy such as Si and C, [42, 43] is effective to improve the thermal stability of glass in both PCM and OTS devices. However, C doping may induce long carbon chains which deviates from the tetrahedral motifs and increases the off-state conductivity (reducing the on/off contrast), while Si is the primary tetrahedral dopant which has been demonstrated to increase thermal stability significantly, [10, 44] even in the commercialized products. [8] Compared to other dopants, Si is distinctive as it enhances thermal stability and endurance while simultaneously reducing V_{th} and V_{th} drift, as demonstrated in **Table S1**. Nevertheless, the atomic mechanisms of Si doping in OTS materials remain ambiguous. Therefore, understanding the atomic mechanisms of Si doping in OTS materials is critical for the design of next-generation high-density 3D PCM. In this study, we employed ab initio calculations to investigate the changes of materials by doping Si, e.g., *a*-GeSe and *a*-GeSiSe (10% Si), focusing on the structural, bonding, and energy bands. Our results indicate that Si doping introduces strong Si-Se and Si-Ge bonds in *a*-GeSiSe. Specifically, the Si-centered clusters exhibit a predominance of tetrahedral shapes, leading to a more distorted local configurations that deviate from the crystalline seeds, e.g., octahedral-like clusters. The decrease of 4-fold rings and atomic movement impedes the crystallization, ensuring the high stability and endurance of the *a*-GeSiSe materials. We also found that the Ge-Ge chains are the

primary contributors to the MGS in both *a*-GeSe and *a*-GeSiSe, while the Si atoms have negligible contribution to lone-pair (LP) electrons and MGS. Moreover, Si doping leads to more stable mid-gap states and thus effectively decreases V_{th} drift coefficient. Our findings provide a comprehensive insight into the effects of Si doping on OTS materials, which is crucial for the design of OTS materials with high stability towards the advancement of high-density memory integration.

2. Methods

The Vienna Ab initio Simulation Package (VASP) code [45] was employed to perform ab initio calculations, and the Perdew-Burke-Ernzerhof generalized gradient approximation (GGA-PBE) exchange functional and projector augmented-wave (PAW) method was utilized. [46, 47] We generate the amorphous models via the Ab initio molecular dynamics (AIMD) based on the density functional theory (DFT). [48] The time step and cutoff energy were set to 3 fs and 300 eV, respectively. Canonical ensemble (NVT) and Nose-Hoover thermostat were adopted to control the pressure and temperature. The initial model was a cubic cell containing 120 Ge and 120 Se atoms, and 10% of Ge and Se atoms were replaced by Si for the GeSiSe alloy. All the models were fully melted at 3000 K for 30 ps to eliminate the memory effect, and then cooled down to 300 K with a cooling rate of 30 K/ps, meanwhile the size of cubic box was adjusted to eliminate external pressure. These models were equilibrated at 300 K for 12 ps to collect the trajectories of atoms. Then all the amorphous models were fully relaxed at 0 K with a force convergence of 0.02 eV to calculate the electronic structure. The energy cutoff was set to 500 eV, and the electronic convergence precisions was 10^{-7} eV. The Brillouin zone was sampled using a 2×2×2 k-points grid. Only the s and p orbitals for Ge, Si and Se are considered in COHP and ICOHP calculations.

3. Results and discussion

3.1. Structural and dynamic properties

To elucidate the role of Si doping in OTS materials, a detailed comparison between *a*-GeSe and *a*-GeSiSe systems is crucial. We calculated the partial pair distribution functions (PDFs) g(r), which characterize the structure of amorphous glass based on the atomic distance, as shown in Fig. 1(a) and 1(b). The dominant Ge-Se peaks in Fig. 1(a) indicate that heteropolar Ge-Se bonds are the primary configuration in the *a*-GeSe model, consistent with our previous findings. [20, 28] In addition, there are a few homopolar Ge-Ge bonds, as evidenced by a small peak of Ge-Ge configuration in Fig. 1(a). Upon Si incorporation into *a*-GeSe, two new peaks of Si-Ge and Si-Se clearly emerge as shown in Fig. 1(b), resulting in a higher amplitude of Ge-Ge peak and a lower amplitude of Ge-Se peak in the *a*-GeSiSe model. This observation is attributed to Si atoms acting as cations, which substitute Ge atoms to bond with Se atoms. The coordination number (CN) distributions for *a*-GeSe and *a*-GeSiSe are shown in Fig. 1(c) and 1(d), respectively. Ge atoms are primarily 4-coordinated and partly 3- and 5-coordinated, while Se atoms are predominantly 3- and 4-coordinated. It indicates that the Si doping has little effect on the coordinated environment of *a*-GeSe. After Si doping, almost all Si atoms exhibit 4-CNs in *a*-GeSiSe, as depicted in Fig. 1(d).

In order to gain a better understanding of the local structure, we computed the bond-angle distribution functions (BADFs) for *a*-GeSe and *a*-GeSiSe, which are depicted in Fig. 1(e) and 1(f). Our findings indicate that in *a*-GeSe, both Ge and Se atoms predominantly form ~90° angles, indicating the defective octahedral motifs. However, upon introducing Si atoms into the *a*-GeSe system, the main peak of Ge atoms shifts to ~96°, indicating that the octahedral-like motifs become more distorted in *a*-GeSiSe. In addition, the main peak of Se atoms has shifted to ~107°, and a second peak is observed at ~88°, indicating the presence of two different structural configurations for Se-centered clusters (tetrahedral-like and octahedral-like). These variations of local structure should stem from Si atoms. As anticipated, the BADFs of Si-centered clusters exhibit a 109° peak, which is the typical feature of a perfect tetrahedron. Our findings suggest that Si doping could enhance the distortion of amorphous structure by transforming it towards tetrahedral-like motifs. As a result, the crystallization process

is inhibited, leading to a higher crystallization temperature for *a*-GeSiSe OTS materials, e.g., an amorphous material with higher thermal stability. The previous work has demonstrated an increase in thermal stability of more than 60 ℃ (from 320 ℃ to 380 ℃) for a-GeSiSe when the Si content is 13 at. %. [44]

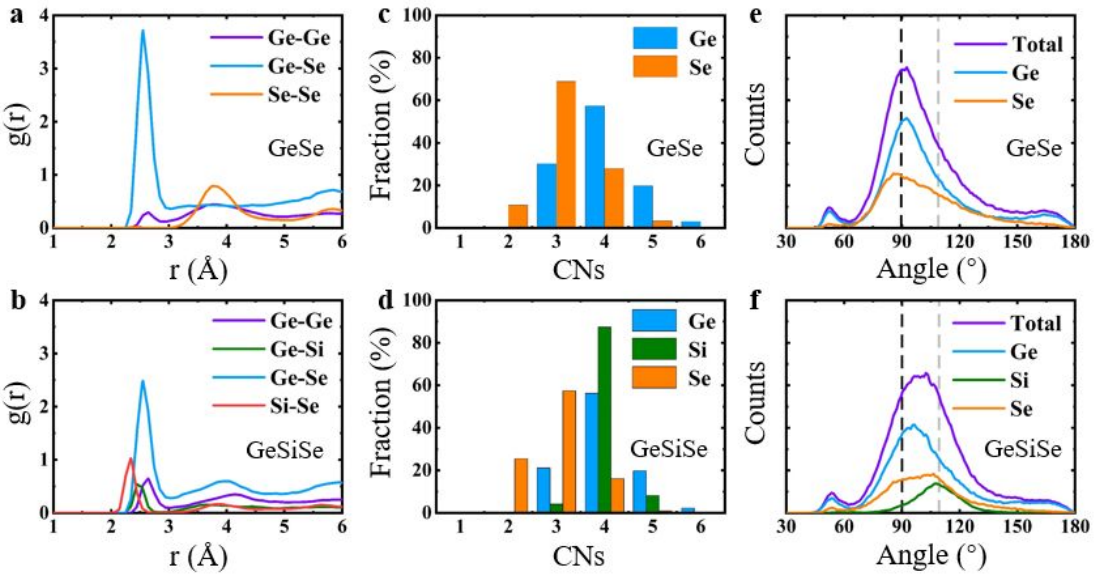

Fig. 1. Local configuration of *a*-GeSe and *a*-GeSiSe. (a-b) Partial pair distribution functions PDFs, (c-d) coordination numbers (CNs) distribution, and (e-f) bond angle distribution function for *a*-GeSe and *a*-GeSiSe. The black and light grey dashed lines in (e) and (f) are located at 90° and 109°, respectively, corresponding to the bond angles of perfect octahedral and tetrahedral configurations.

The presence of tetrahedral Si-centered atomic clusters in *a*-GeSiSe can be clearly observed in the simulated amorphous models, as shown in Fig. 2(a). In these models, Si-centered tetrahedrons are randomly distributed in the amorphous state without showing significant aggregation, and they form clusters that deviate from the parent *a*-GeSe structure, contributing to the disorder of doped glass. To determine the fraction of distorted tetrahedrons of Si-centered motifs, the order parameter q was calculated using the following equation, [49]

$$q = 1 - \frac{3}{8}\sum_{i>k}\left(\frac{1}{3} + \cos\theta_{ijk}\right)^2 \qquad (1)$$

where θ_{ijk} denotes the bond angle formed by the central atom *j* with each neighboring atom *i* and atom *k*, and the sum counts all pair atoms (atom *i*, atom *k*) bonded to a central atom *j*. For 4-coordinated motifs, the motifs with *q* values between 0.8 and 1.0 are considered to be tetrahedrons with slight distortions, while the *q* value of 1.0 represented perfect tetrahedrons without any distortion. As shown in Fig. 2(b), 85.8% 4-coordinated Si form tetrahedron motifs. Noted that Ge atoms in amorphous chalcogenides glasses (PCM or OTS) could also form tetrahedral motifs according to previous reports. [50, 51] To distinguished the source of tetrahedral clusters in *a*-GeSiSe, the distribution of the *q* parameter for 4-coordinated Ge was also calculated for both *a*-GeSe and *a*-GeSiSe. As shown in Fig. 2(c), the fraction of tetrahedral Ge-centered motifs increased from 22.5% to 27.5% upon Si doping, indicating high probability for forming tetrahedral structures (extra Si-centered and pristine Ge-centered) in OTS materials.

The primitive rings, which are defined as rings connected by atoms and are related to crystallization behavior, could also be indicative of thermal stability. Using the RINGS code, [52] the distribution of rings for *a*-GeSe and *a*-GeSiSe was obtained, as shown in Fig. 2(d). The largest amount of rings in *a*-GeSe are 4-fold rings, which are associated with rapid crystallization of PCM because they resembles the local structure of rocksalt crystals. [53] However, by adding Si into *a*-GeSe, the proportion of 4-fold rings decreases and 5-fold rings become more prominent in *a*-GeSiSe. This is also an indication that Si can suppress the crystallization process based on quadruple nuclei, resulting in a high thermal stability of the glass.

The failure of OTS devices is mainly attributed to crystallization or phase separation of glass, as shown in previous research. [10] The dynamic properties of materials, particularly atomic migration, are closely linked to their ability to undergo phase transformation or separation. In this study, we investigated the effect of Si doping on the dynamic properties of OTS materials by calculating the mean squared displacement (MSD). The atomic migration was evaluated using the following equation:

$$\left\langle R_\alpha^2(t)\right\rangle = \frac{1}{N_\alpha}\left\langle \sum_{i=1}^{N_\alpha} \left|R_{i\alpha}(t+\tau) - R_{i\alpha}(\tau)\right|^2 \right\rangle \qquad (2)$$

where N_α denotes the total number of α atoms, τ represents the arbitrary origin of time and $R_{i\alpha}$ denotes the coordinates of atom i. Fig. 2(e) and 2(f) show the MSD curves of various elements for *a*-GeSe and *a*-GeSiSe at 600 K over a period of 12 ps, respectively. As shown in Fig. 2(e), the MSD curves of Ge and Se in *a*-GeSe almost overlap, indicating similar atomic mobility for both elements. However, upon adding Si to *a*-GeSe, the MSD curves of Ge and Se show a reduction in amplitude by half, with the MSD of Se being slightly lower than that of Ge. Notably, Si in *a*-GeSiSe exhibits the lowest mobility, suggesting that atomic movement is significantly hindered. Such a high activation energy of diffusion could hinder the phase separation and crystallization behavior of OTS materials. Consequently, the endurance and thermal stability of *a*-GeSiSe OTS glass are improved. Previous work has shown nearly two orders magnitude of endurance improvement after Si doping, 10^5 cycles for a-$Ge_{42}Se_{58}$ and 5×10^6 cycles for a-GeSiSe with 13 at. % Si content. [44] This sluggish atomic mobility could be attributed to the formation of stronger Si-Se and Si-Ge bonds.

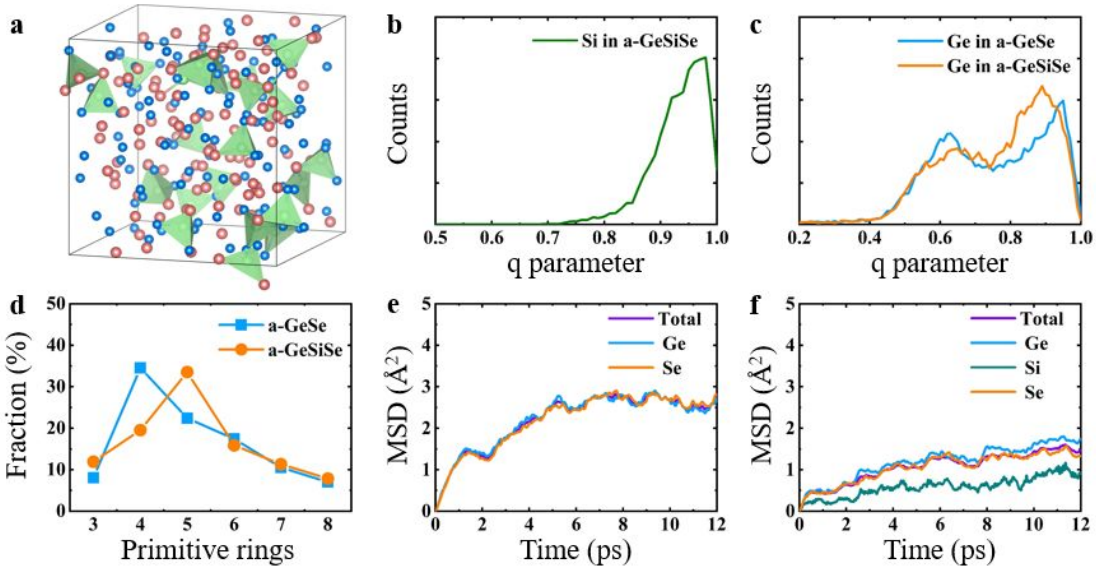

Fig. 2. Local structure parameters and dynamic properties of *a*-GeSe and *a*-GeSiSe. (a) The distribution of Si-centered tetrahedrons in *a*-GeSiSe. The orange, green and blue balls in (a) represent Ge, Si and Se atoms. (b-c) Local order parameter *q* of 4-

coordinated Si and Ge, respectively, showing obvious tetrahedral motifs because of q value predominately located at 0.8-1.0. (d) Ring distributions of *a*-GeSe and *a*-GeSiSe, showing the proportions of 4-fold rings decreases in a-GeSiSe. (e) and (f) mean square displacement (MSD) of *a*-GeSe and *a*-GeSiSe, respectively, indicating atomic movement is significantly hindered upon Si doping.

3.2. Bonding analysis of amorphous glass

To reveal the influence of Si doping on atomic motion and thermal stability, we investigated the chemical bonds including the charge transfer and bond strength. We utilized the Bader Charge code [54] to compute the charge transfer of different elements in *a*-GeSe and *a*-GeSiSe, as shown in Fig. 3(a) and 3(b), where the +/- signs indicate the gain or loss of valence electrons. In *a*-GeSe, the average charge transfer of Ge and Se was calculated to be -0.59 and +0.59, respectively. Upon Si doping, the average charge transfer values of Ge and Se become -0.42 and +0.66, respectively, while Si loses ~1.06 valence electrons on average, indicating that Si doping strengthens the ionicity of the chemical bonds. Furthermore, compared with *a*-GeSe, the charge transfer becomes more dispersed in *a*-GeSiSe, which might be attributed to the structural distortion resulting from Si incorporation.

To directly investigate the effect of Si on the bond strength, we utilized the LOBSTER code to calculate the crystal orbital Hamilton populations (COHP) of *a*-GeSiSe. [55, 56] In general, negative values below the Fermi level represent antibonding states, while positive values indicate bonding states for -COHP. The -COHP of various bonds in *a*-GeSiSe is shown in Fig. 3(c), where both Ge-Se and Si-Se bonds show antibonding states. But Si-Se has less antibonding state, thus is stronger than Ge-Se. To quantitatively compare the strength of chemical bonds, we calculated the integrated -COHP (-ICOHP) below the Fermi level, which could sum up both bonding and antibonding contribution. Fig. 3(d) displays the -ICOHP of all the bonds, and the red stars represent the average bonding strength of the main bond lengths (the first peak of PDFs). The -ICOHP values of Ge-Ge, Ge-Si, Ge-Se, and Si-Se were identified to be

3.4 eV, 4.1 eV, 3.6 eV, and 5.1 eV, respectively. It suggests that the Ge-Si and Si-Se bonds are stronger than Ge-Se, leading to the enhanced stability and high endurance of the *a*-GeSiSe.

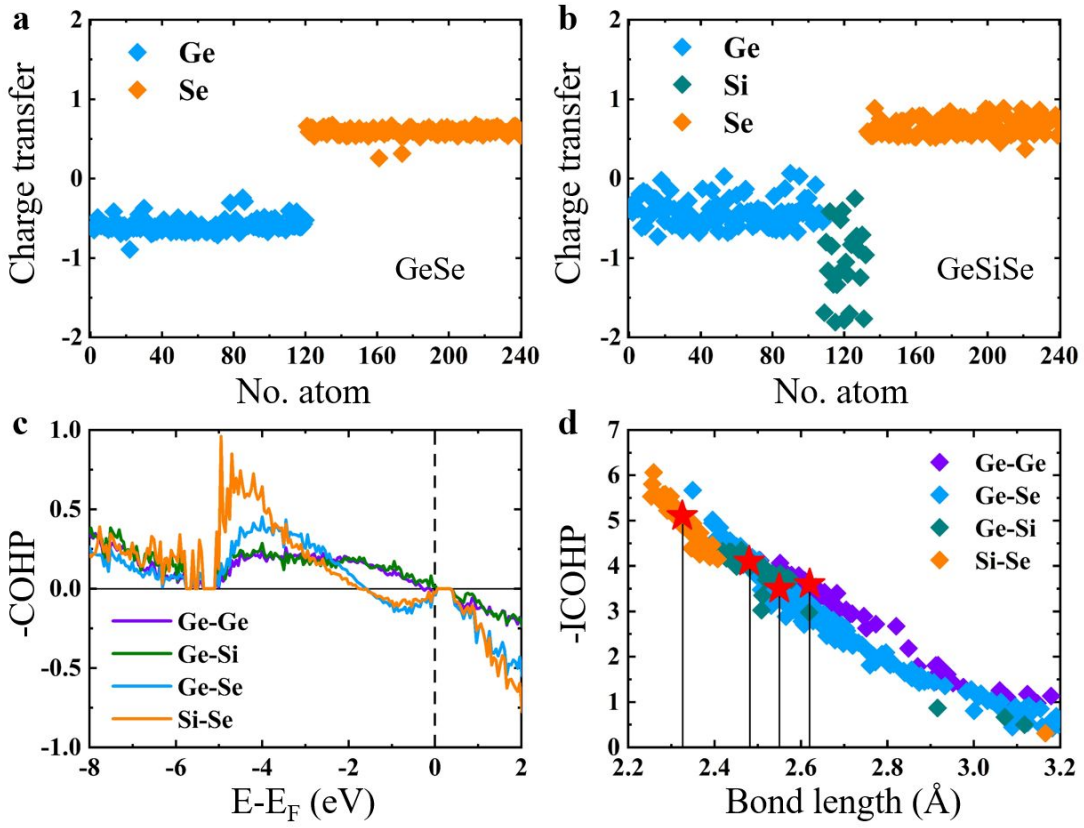

Fig. 3. Charge transfer and bonding analysis for *a*-GeSe and *a*-GeSiSe. The Bader charge transfer for (a) *a*-GeSe and (b) *a*-GeSiSe, where the +/– symbol represents gain/loss of electrons. (c) The -COHP for different bonds in *a*-GeSiSe. (d) The -ICOHP for different bonds with corresponding length in *a*-GeSiSe. The red stars correspond to the interatomic distances for the first peaks of the PDFs in Fig. 1(a-b).

3.3. Voids and lone pair electrons

The void distribution is a notable structural feature that relates to the electronic properties, as increasing voids could open the band gap. To quantify the volume of voids in the amorphous models, we used a method based on electron density. [57] The distributions of normalized electron density (D^e_{norm}) for *a*-GeSe and *a*-GeSiSe are displayed in Fig. 4(a), and the void concentration is calculated by integrating the LED

regions and setting the boundary between LED and high electron density (HED) areas to 0.22, as in our previous study. [20, 58] The results indicate that both *a*-GeSe and *a*-GeSiSe possess voids with volume fractions of 26.4% and 25.4%, respectively, suggesting that Si doping has little influence on the voids. Fig. 4(b) and 4(c) display the distributions of void in *a*-GeSe and *a*-GeSiSe models, respectively. These voids are randomly distributed in the amorphous models and act like a van der Waals layer in crystal GeSe (*c*-GeSe), inhibiting atomic migration. [53, 59]

To further reveal the nature of amorphous void distribution, we investigated the distribution of LP electrons. According to previous reports, not only the voids but also the MGS stems from the LP electrons. [25, 27] The behavior of LP electrons, which are already paired and do not participate in covalent bonding, is critical to the operation of OTS under an electric field due to their higher energies than bonded electrons. [25] Therefore, it is worthwhile to explore the LP electrons of *a*-GeSe and *a*-GeSiSe. We computed the electron localization function (ELF) distributions to exhibit the distribution of LP electrons as shown in Fig. 4(d). In general, ELF values close to 1.0 indicate highly localized covalent bonds, while those closer to 0.5 indicate metallic bonds with delocalized electrons. By integrating the ELF value between 0.85 (Fig. S1) and 1.0, we determined the fractions of LP electrons, which are 7.8% and 7.2% for *a*-GeSe and *a*-GeSiSe, respectively. [60] These results indicate that Si doping reduces the fraction of LP electrons in amorphous models. The ELF distributions with an isovalue of 0.85 are presented in Fig. 4(e) and 4(f) for *a*-GeSe and *a*-GeSiSe, respectively. We observed that in *a*-GeSe, most of the electron clouds were located at the opposite side of the bonding area near Se atoms, suggesting that the LP electrons mostly originate from Se atoms, as expected. Notably, some LP electrons appeared around the Ge atoms, likely due to over-coordinated Ge configurations. When Si is added to *a*-GeSe, the LP electrons are still primarily located around Se and Ge atoms, similar to *a*-GeSe. However, they are hardly found near Si atoms, indicating that Si atoms made little contribution to the LP electrons.

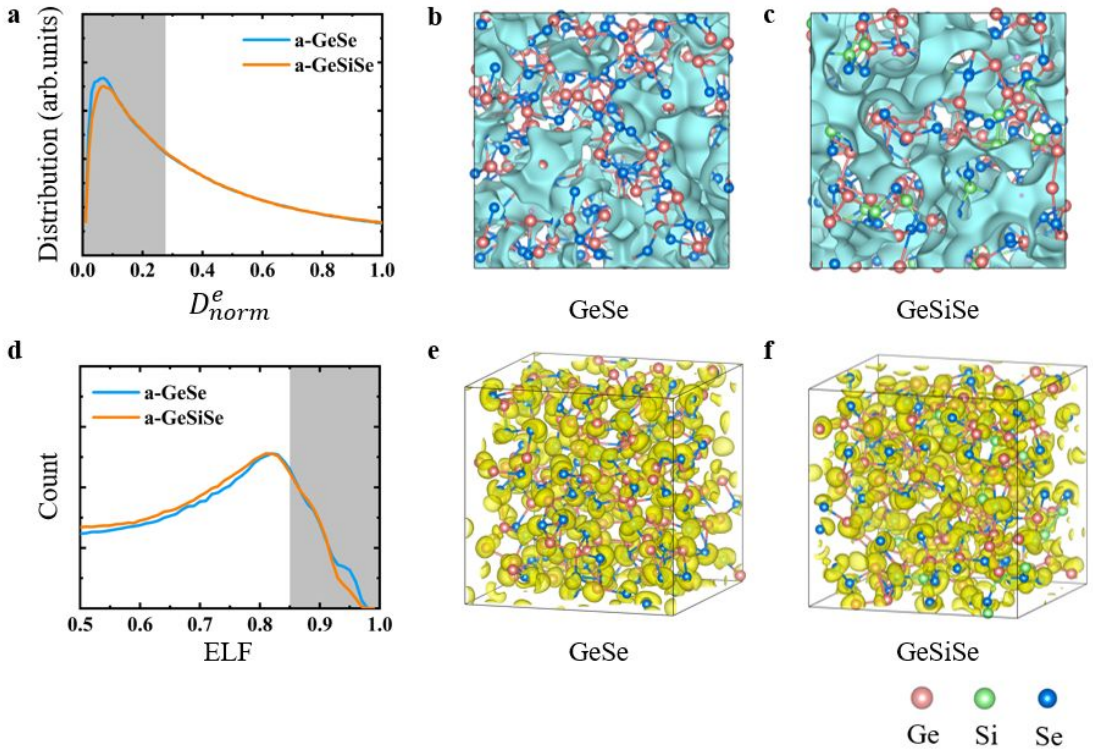

Fig. 4. Voids and lone-pair electron for *a*-GeSe and *a*-GeSiSe. (a) The distribution of normalized electron density of *a*-GeSe and *a*-GeSiSe. (b) and (c) show the distributions of low electron density (LED) region with an isovalue of 0.0035 e×bohr^{-3} in *a*-GeSe and *a*-GeSiSe. (d) the distribution of normalized electron localized function (ELF) for *a*-GeSe and *a*-GeSiSe. (e) and (f) shows the associated distribution of ELF with an isovalue of 0.85 for *a*-GeSe and *a*-GeSiSe, which mainly located at the opposite side of covalent bonds near Ge and Se atoms.

3.4. Nature of mobility gap states

To determine the relationship between Si doping and MGS, we calculated the electronic density of states (DOS) and corresponding normalized inverse participation ratio (IPR) for *a*-GeSe and *a*-GeSiSe as shown in Fig. 5(a) and 5(c). The IPR values reflect the degree of localization of electron states, as higher IPR values suggest more localized electron states. The mobility gap of amorphous glass is determined by calculating the distance between the valence and conduction bands, which are defined by relatively

lower IPR values. [61] The mobility gap is slightly different from regular band gap because the former does not count the band tails. Our calculations reveal that the mobility gaps for a-GeSe and a-GeSiSe are 1.08 eV and 0.9 eV, respectively, which is consistent with experimental findings.[44] In these experiments, the mobility gap was shown to be 1.12 eV for a-$Ge_{42}Se_{58}$ and 0.90 eV for a-GeSiSe with 13 at. % Si content, demonstrating a decreasing trend in the mobility gap. These results suggest that Si doping could reduce the mobility gap of *a*-GeSe, which may lead to increased leakage current and reduced V_{th}, because the V_{th} is positively related to the mobility gap according to the PF model. [31] The previous work has demonstrated the 0.5 V (from 2.5 V to 2.0 V) reduction of V_{th} when adding 13 at. % Si content into a-Ge42Se58. [44] In both *a*-GeSe and *a*-GeSiSe models, MGS with higher IPR values associated with OTS behavior are observed. Although the carriers trapped in MGS contribute little to room temperature conductivity, they would tunnel to the mobility edge and significantly reduce resistance when the electrical field is applied.

Using analytical methods for electron wave-functions, we have projected the mid-gap states (MGS) onto real space to determine their origin, as shown in Fig. 5(b) and 5(d). The figures show that the MGS mainly originates from structural motifs consisting of Ge-Ge chains that break the "8-*N*" rule (also known as octet rule, refers to for each N_{th} group nonmetallic element, each atom could provide 8-N valence electrons to form 8-N covalent bonds with 8-N neighboring atoms), consistent with previous works. [21] Interestingly, we find that Si atoms fail to significantly contribute to the MGS, which is in line with our conclusions about the localization of LP electrons. Furthermore, the evolution of MGS could be related to V_{th} drift, [21, 40] which is caused by the Ge-Ge bonds in chalcogenide glass. [40, 62] Experimental studies have reported a decrease in the coefficient of V_{th} drift after Si doping into the *a*-GeSe material. [44] To clarify this phenomenon, we compared the Ge-Ge bonds in *a*-GeSe with *a*-GeSiSe, as displayed in Fig. 5(e). And we also tested different annealing rates to compare the number of Ge-Ge bonds, as shown in Table. S2. Our analysis reveals that the Ge-Ge bonds in *a*-GeSiSe have fewer antibonding states than in *a*-GeSe, indicating that they are more stable.

Hence, the stable amorphous structure could inhibit the evolution of MGS and V_{th} drift. The previous work has shown V_{th} ranges from 2.3 V to 2.7 V for a-$Ge_{42}Se_{58}$ and 1.85 V to 2.1 V for a-GeSiSe with 13 at. % Si contents, demonstrating that Si doping to a-GeSe could effectively improve the amorphous stability. [44] Additionally, the strong Ge-Si and Si-Se bonds could potentially suppress the V_{th} drift because they slow down the ageing of glass.

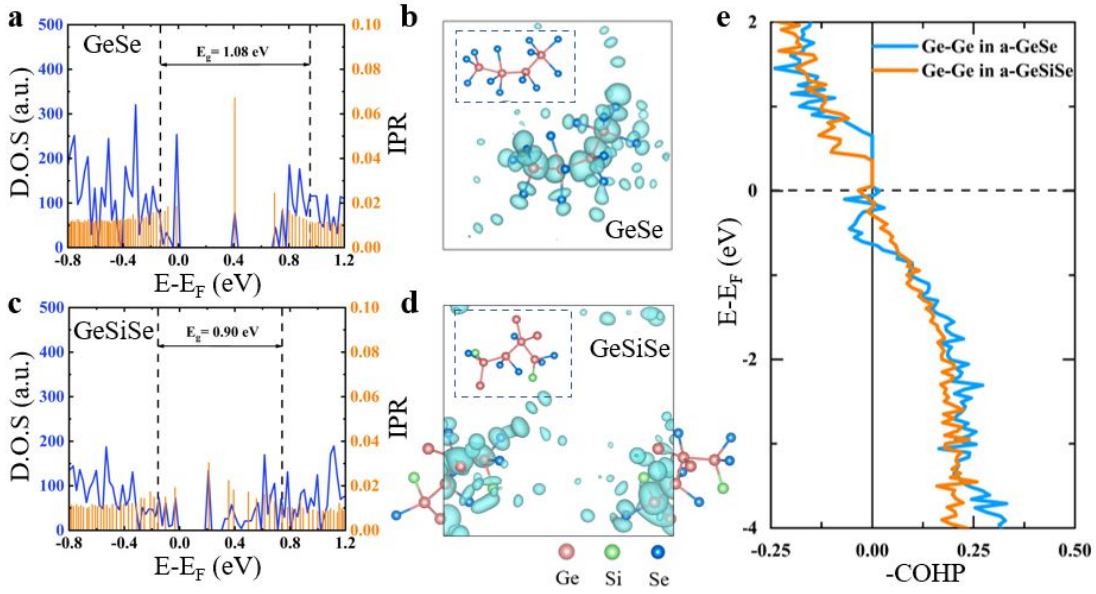

Fig. 5. Electronic structure and the mid-gap states for *a*-GeSe and *a*-GeSiSe. (a) and (c) density of states (DOS) and normalized inverse participation ratio (IPR) of *a*-GeSe and *a*-GeSiSe, respectively. (b) and (d) the mid gap states (MGS) projected onto real space, in which the blue regions represent the molecular-orbital-charge density of the associated MGS, and the main atomic configurations in dashed box associated with the MGS. (e) The -COHP for Ge-Ge bonds in *a*-GeSe and *a*-GeSiSe.

4. Conclusions

In summary, we systematically investigated the structural, dynamic, and electronic properties of *a*-GeSe and *a*-GeSiSe to elucidate the impact of Si doping on the stability, endurance, V_{th}, and leakage of OTS materials. Our findings indicate that Si atoms form strong Si-Se and Si-Ge bonds that impede atomic movement, with Si-centered clusters

predominantly forming stiff tetrahedral cluster. Local configurations distorted from the octahedral-like motifs are enhanced substantially in *a*-GeSiSe. Furthermore, *a*-GeSiSe exhibits a higher proportion of Ge-centered tetrahedrons and 5-fold rings, resulting in higher stability of the amorphous glass. The Ge-Ge bonds in *a*-GeSiSe are more stable, leading to a lower V_{th} drift coefficient. Finally, the contribution of Si atoms to LP electrons and mid-gap states is negligible, indicating that Si doping may have limited negative effects on OTS performance. Our study sheds light on the intricate structure-property relationships in amorphous chalcogenide glass and offers insights for designing and developing OTS materials with high stability, endurance, and low V_{th} drift.

Conflicts of interest

The authors declare that they have no known competing financial interests or personal relationships that could have appeared to influence the work reported in this paper.

Acknowledgements

This work was supported by National Key R&D Program of China (Grant No. 2022ZD0117600); M.X. acknowledges the National Natural Science Foundation of China (Grant No. 62174060) and the Fundamental Research Funds for the Central Universities, HUST (No. 2021GCRC051). Work at Ames Laboratory was supported by the U.S. Department of Energy (DOE), Office of Science, Basic Energy Sciences, Materials Science and Engineering Division including a grant of computer time at the National Energy Research Scientific Computing Centre (NERSC) in Berkeley, CA. Ames Laboratory is operated for the U.S. DOE by Iowa State University under Contract No. DE-AC02-07CH11358.

References

1. M. Wuttig, D. Lusebrink, D. Wamwangi, W. Welnic, M. Gillessen and R. Dronskowski, *Nat. Mater.*, 2007, **6**, 122-128.
2. S. Raoux, W. Wełnic and D. Ielmini, *Chem. Rev.*, 2010, **110**, 240-267.
3. W. Zhang, R. Mazzarello, M. Wuttig and E. Ma, *Nat. Rev. Mater.*, 2019, **4**, 150-168.
4. Y. T. Liu, X. B. Li, H. Zheng, N. K. Chen, X. P. Wang, X. L. Zhang, H. B. Sun and S. Zhang, *Adv. Funct. Mater.*, 2021, **31**, 2009803.
5. M. Xu, X. Mai, J. Lin, W. Zhang, Y. Li, Y. He, H. Tong, X. Hou, P. Zhou and X. Miao, *Adv. Funct. Mater.*, 2020, **30**, 2003419.
6. K. Li, B. Liu, J. Zhou, S. R. Elliott and Z. Sun, *Acta Mater.*, 2023, **249**, 118809.
7. J. Shen, W. Song, K. Ren, Z. Song, P. Zhou and M. Zhu, *Adv. Mater.*, 2023, **35**, 2208065.
8. J. Hruska, Intel, Micron reveal Xpoint, a new memory architecture that could outclass DDR4 and NAND, https://www.extremetech.com/extreme/211087-intel-micron-reveal-xpoint-a-new-memory-architecture-that-claims-to-outclass-both-ddr4-and-nand, (accessed July 28,, 2015).
9. J. Choe, Intel 3D XPoint Memory Die Removed from Intel Optane™ PCM (Phase Change Memory), https://www.techinsights.com/blog/intel-3d-xpoint-memory-die-removed-intel-optanetm-pcm-phase-change-memory, (accessed May 18,, 2017).
10. M. Zhu, K. Ren and Z. Song, *MRS Bull.*, 2019, **44**, 715-720.
11. J. Shen, S. Jia, N. Shi, Q. Ge, T. Gotoh, S. Lv, Q. Liu, R. Dronskowski, S. R. Elliott and Z. Song, *Science*, 2021, **374**, 1390-1394.
12. R. Gu, M. Xu, R. Yu, C. Qiao, C.-Z. Wang, K.-M. Ho, S. Wang, X. Miao and M. Xu, *APL Mater.*, 2021, **9**, 081101.
13. A. D. Franklin, *Science*, 2015, **349**, aab2750.
14. S. R. Ovshinsky, *Phys. Rev. Lett.*, 1968, **21**, 1450.
15. Y. Koo, K. Baek and H. Hwang, 2016 IEEE Symposium on VLSI Technology, Honolulu, HI, USA, 2016.
16. L. Wang, W. Cai, D. He, Q. Lin, D. Wan, H. Tong and X. Miao, *IEEE Electron Device Lett*, 2021, **42**, 688-691.
17. D. Garbin, W. Devulder, R. Degraeve, G. L. Donadio, S. Clima, K. Opsomer, A. Fantini, D. Cellier, W. G. Kim and M. Pakala, 2019 IEEE International Electron Devices Meeting (IEDM), San Francisco, CA, USA, 2019.
18. H.-Y. Cheng, I. Kuo, W. Chien, C. Yeh, Y. Chou, N. Gong, L. Gignac, C. Yang, C. Cheng and C. Lavoie, 2020 IEEE Symposium on VLSI Technology, Honolulu, HI, USA, 2020.
19. H. Cheng, W. Chien, I. Kuo, C. Yeh, L. Gignac, W. Kim, E. Lai, Y. Lin, R. Bruce and C. Lavoie, 2018 IEEE International Electron Devices Meeting (IEDM), San Francisco, CA, USA, 2018.
20. R. Gu, M. Xu, C. Qiao, C.-Z. Wang, K.-M. Ho, S. Wang, M. Xu and X. Miao, *Scr. Mater.*, 2022, **218**, 114834.
21. S. Clima, B. Govoreanu, K. Opsomer, A. Velea, N. S. Avasarala, W. Devulder, I. Shlyakhov, G. L. Donadio, T. Witters, S. Kundu, L. Goux, V. Afanasiev, G. S. Kar and G. Pourtois, 2017 IEEE International Electron Devices Meeting (IEDM), San Francisco, CA, USA, 2017.

22. S. Jia, H. Li, T. Gotoh, C. Longeaud, B. Zhang, J. Lyu, S. Lv, M. Zhu, Z. Song, Q. Liu, J. Robertson and M. Liu, *Nat. Commun.*, 2020, **11**, 4636.
23. R. Wu, S. Jia, T. Gotoh, Q. Luo, Z. Song and M. Zhu, *Adv. Electron. Mater.*, 2022, **8**, 2200150.
24. T. Kaplan and D. Adler, *Appl. Phys. Lett.*, 1971, **19**, 418-420.
25. M. Kastner, D. Adler and H. Fritzsche, *Phys. Rev. Lett.*, 1976, **37**, 1504.
26. S. Menzel, U. Böttger, M. Wimmer and M. Salinga, *Adv. Funct. Mater.*, 2015, **25**, 6306-6325.
27. K. Konstantinou, F. C. Mocanu, T. H. Lee and S. R. Elliott, *Nat. Commun.*, 2019, **10**, 3065.
28. M. Xu, M. Xu and X. Miao, *InfoMat*, 2022, **4**, e12315.
29. M. Xu, Q. Xu, R. Gu, S. Wang, C. Z. Wang, K. M. Ho, Z. Wang, M. Xu and X. Miao, *Adv. Funct. Mater.*, 2023, 2304926.
30. D. Adler, M. Shur, M. Silver and S. Ovshinsky, *J. Appl. Phys.*, 1980, **51**, 3289-3309.
31. D. Ielmini and Y. Zhang, *J. Appl. Phys.*, 2007, **102**, 054517.
32. D. M. Kroll, *Phys. Rev. B*, 1974, **9**, 1669.
33. V. Karpov, Y. Kryukov, I. Karpov and M. Mitra, *Phys. Rev. B*, 2008, **78**, 052201.
34. V. Karpov, Y. Kryukov, S. Savransky and I. Karpov, *Appl. Phys. Lett.*, 2007, **90**, 123504.
35. Z. Chai, W. Zhang, S. Clima, F. Hatem, R. Degraeve, Q. Diao, J. F. Zhang, P. Freitas, J. Marsland and A. Fantini, *IEEE Electron Device Lett*, 2021, **42**, 1448-1451.
36. J. Kim, W. Kim, J. Kim and H. Sohn, *AIP Advances*, 2023, **13**, 035221.
37. N. S. Avasarala, G. L. Donadio, T. Witters, K. Opsomer, B. Govoreanu, A. Fantini, S. Clima, H. Oh, S. Kundu, W. Devulder, M. H. v. d. Veen, J. V. Houdt, M. Heyns, L. Goux and G. S. Kar, 2018 IEEE Symposium on VLSI Technology, Honolulu, HI, USA, 2018.
38. D. Ielmini and Y. Zhang, *Appl. Phys. Lett.*, 2007, **90**, 192102.
39. C. Qiao, M. Xu, S. Wang, C.-Z. Wang, K.-M. Ho, X. Miao and M. Xu, *Scr. Mater.*, 2021, **202**, 114011.
40. S. Clima, D. Garbin, W. Devulder, J. Keukelier, K. Opsomer, L. Goux, G. S. Kar and G. Pourtois, *Microelectron. Eng.*, 2019, **215**, 110996.
41. M. Anbarasu, M. Wimmer, G. Bruns, M. Salinga and M. Wuttig, *Appl. Phys. Lett.*, 2012, **100**, 143505.
42. M. Xu, B. Li, K. Xu, H. Tong, X. Cheng, M. Xu and X. Miao, *Phys. Chem. Chem. Phys.*, 2019, **21**, 4494-4500.
43. L. Tong, L. Xu, Y. Jiang, F. Yang, L. Geng, J. Xu, W. Su, Z. Ma and K. Chen, *J. Non-Cryst. Solids*, 2012, **358**, 2402-2404.
44. X. Li, Z. Yuan, S. Lv, S. Song and Z. Song, *Thin Solid Films*, 2021, **734**, 138837.
45. Kresse and Furthmuller, *Phys. Rev. B*, 1996, **54**, 11169-11186.
46. J. Perdew, K. Burke and M. Ernzerhof, *Phys. Rev. Lett.*, 1996, **77**, 3865-3868.
47. P. E. Blöchl, *Phys. Rev. B*, 1994, **50**, 17953.
48. J. Hafner, *J. Comput. Chem.*, 2008, **29**, 2044-2078.
49. J. R. Errington and P. G. Debenedetti, *Nature*, 2001, **409**, 318-321.
50. R. Mazzarello, S. Caravati, S. Angioletti-Uberti, M. Bernasconi and M. Parrinello, *Phys. Rev. Lett.*, 2010, **104**, 085503.
51. S. Caravati, M. Bernasconi, T. D. K hne, M. Krack and M. Parrinello, *Appl. Phys. Lett.*, 2007, **91**, 171906.
52. S. Roux and P. Jund, *Comput. Mater. Sci.*, 2010, **49**, 70-83.
53. T. H. Lee and S. R. Elliott, *Phys. Rev. Lett.*, 2011, **107**, 145702.

54. W. Tang, E. Sanville and G. Henkelman, *J. Phys.-Condes. Matter*, 2009, **21**, 084204.
55. R. Nelson, C. Ertural, J. George, V. L. Deringer, G. Hautier and R. Dronskowski, *J. Comput. Chem.*, 2020, **41**, 1931-1940.
56. R. Dronskowski and P. E. Bloechl, *J. Phys. Chem.*, 1993, **97**, 8617-8624.
57. M. Xu, Y. Cheng, L. Wang, H. Sheng, Y. Meng, W. Yang, X. Han and E. Ma, *Proc. Natl. Acad. Sci.*, 2012, **109**, E1055-E1062.
58. M. Xu, Y. Q. Cheng, H. W. Sheng and E. Ma, *Phys. Rev. Lett.*, 2009, **103**, 195502.
59. Z. Sun, J. Zhou, A. Blomqvist, B. Johansson and R. Ahuja, *Phys. Rev. Lett.*, 2009, **102**, 075504.
60. J.-Y. Raty, C. Gatti, C.-F. Schoen and M. Wuttig, *Phys. Status Solidi-Rapid Res. Lett.*, 2021, **15**, 2000534.
61. S. Clima, T. Ravsher, D. Garbin, R. Degraeve, A. Fantini, R. Delhougne, G. S. Kar and G. Pourtois, *ACS Appl. Electron. Mater.*, 2023, **5**, 461-469.
62. W. Zhang and E. Ma, *Mater. Today*, 2020, **41**, 156-176.